

Accretion mediated spin-eccentricity correlations in LISA massive black hole binaries

Mudit Garg,^{1*} Christopher Tiede,² & Daniel J. D’Orazio^{2,3}

¹*Department of Astrophysics, University of Zurich, Winterthurerstrasse 190, CH-8057 Zürich, Switzerland*

²*Niels Bohr International Academy, Niels Bohr Institute, Blegdamsvej 17, 2100 Copenhagen, Denmark*

³*Space Telescope Science Institute, 3700 San Martin Drive, Baltimore, MD 21218, USA*

Accepted ????. Received ????. in original form ???.

ABSTRACT

We examine expected effective spin ($\chi_{\text{eff},1\text{yr}}$) and orbital eccentricity ($e_{1\text{yr}}$) correlations for a population of observable equal-mass massive black hole binaries (MBHBs) with total redshifted mass $M_z \sim [10^{4.5}, 10^{7.5}] M_\odot$ embedded in a circumbinary disc (CBD) at redshifts $z = 1$ and $z = 2$, one-year before merging in the LISA band. We find a strong correlation between measurable eccentricity and negative effective spin for MBHBs that are carried to merger by retrograde accretion. This is due to the well-established eccentricity pumping of retrograde accretion and less-well-established formation of retrograde minidisks coupled with a stable retrograde CBD throughout the binary evolution from the self-gravitating radius. Conversely, prograde accretion channels result in positive $\chi_{\text{eff},1\text{yr}}$ and non-measurable $e_{1\text{yr}}$ except for almost unity Eddington ratio and $M_z \lesssim 10^5 M_\odot$ MBHBs at $z = 1$. This clear contrast between the two CBD orientations – and particularly the unique signature of retrograde configurations – provides a promising way to unlock the mysteries of MBHB formation channels in the LISA era.

Key words: accretion, accretion discs – black hole mergers – gravitational waves – methods: numerical – quasars:general

1 INTRODUCTION

Galaxy mergers in the Universe lead to the formation of massive black hole binaries (MBHBs; Begelman et al. 1980). Dynamical friction from stars and gas can bring such MBHBs to parsec scales, but beyond this it becomes inefficient. At these separations, gravitational waves (GWs) alone can not merge the binary within the lifetime of the Universe. This is canonically referred to as the final-parsec problem (Milosavljevic & Merritt 2003). However, there are several possibilities suggested to overcome this problem such as improvements in modeling stellar potentials (see, e.g. Preto et al. 2011; Khan et al. 2011; Vasiliev et al. 2015), subsequent galactic mergers, and gas discs around binaries (see, e.g., Amaro-Seoane et al. 2023), but how this is overcome in nature remains uncertain. These dynamical effects can shrink MBHBs through the sub-parsec regime until GWs become strong enough to drive the binary to merger within a Hubble time. Recently, pulsar timing arrays (EPTA Collaboration et al. 2023; Agazie et al. 2023; Reardon et al. 2023; Xu et al. 2023) have provided evidence for a stochastic GW background that is likely sourced by a population of $\gtrsim 10^8 M_\odot$ inspiraling MBHBs, which have made it through the final parsec. If this also occurs for $10^4 - 10^8 M_\odot$ near-equal-mass merging MBHBs, then they will be observable up to redshift $z \sim 20$ by the Laser Interferometer Space Antenna (LISA; Amaro-Seoane et al. 2017; Colpi et al. 2024), recently adopted by ESA, together with in-development TianQin (Li et al. 2024) and Taiji (Gong et al. 2021).

In the LISA milli-Hz-frequency band, GWs from MBHBs will have high signal-to-noise ratios (SNRs), which will help to constrain source parameters and also put constraints on merging binaries’ environments. The effects of gas are particularly compelling because they can simultaneously provide electromagnetic (EM) counterparts (Haiman 2017; Mangiagli et al. 2022; D’Orazio & Charisi 2023; Franchini et al. 2024; Cocchiararo et al. 2024) and leave detectable imprints on the GW waveform in LISA. For the latter, gas has been demonstrated to alter the binary inspiral rate (Garg et al. 2022; D’Orazio & Duffell 2021; Garg et al. 2024c; Tiede & D’Orazio 2024), to produce measurable residual orbital eccentricities (Roedig & Sesana 2014; Zrake et al. 2021; Tiede & D’Orazio 2024; Fumagalli & Gerosa 2023; Garg et al. 2024b), and to impact the magnitude and orientation of the component BH spins (Bardeen 1970; Thorne 1974; Bardeen & Petterson 1975). Similar to gas, stellar hardening (Quinlan 1996; Khan et al. 2011; Gualandris et al. 2022) and three-body interactions (Blaes et al. 2002; Bonetti et al. 2019) can produce measurable residual binary eccentricities, but only the latter can additionally alter the component BH spin orientation (Liu & Lai 2017). Lastly, ignoring even mild gas effects or small orbital eccentricity when modeling MBHBs in the LISA band can suggest false violations of general relativity (Garg et al. 2024a).

In the classical picture for massive binary accretion, radiatively efficient gas settles into a co-planar circumbinary disc (CBD; D’Orazio et al. 2016) with prograde (retrograde) CBDs leading to CBD-aligned mini-discs around each component BH (e.g. Farris et al. 2014; Tiede & D’Orazio 2024). Recent suites of high-resolution hydrodynamical simulations of CBDs suggest pumping or damping of binary orbital eccentricity depending on binary and disc parameters. In particular,

* E-mail: mudit.garg@uzh.ch

whether the disc settles into a prograde or retrograde configuration can have an important impact on the binary eccentricity evolution, and the rate at which the binary inspirals (if at all; see, *e.g.*, Muñoz et al. 2019) which could lead to distinguishable parameters in the LISA band for the same starting binary. For prograde accretion scenarios (Zrake et al. 2021; D’Orazio & Duffell 2021; Siwek et al. 2023), gas brings the binary to an equilibrium eccentricity ~ 0.4 , where it shrinks the binary’s semi-major axis until GWs are strong enough to drive the binary to coalescence, circularizing the orbit (Peters & Mathews 1963; Peters 1964). In retrograde configurations (Bankert et al. 2015; Schnittman & Krolik 2015; Tiede & D’Orazio 2024), there is an eccentricity pumping throughout the evolution until the GWs takeover (but, see also Nixon et al. 2011a; Roedig & Sesana 2014 for low-eccentricity behavior). In retrograde discs, the binary also shrinks its semi-major axis at least two-times more quickly than in prograde scenarios leading to the possibility of different final masses, spins of the component BHs (Dotti et al. 2010; Miller & Krolik 2013), and orbital eccentricity (Roedig et al. 2011; Schnittman & Krolik 2015; Zrake et al. 2021) near-coalescence for the same starting binary.

A recent study (Garg et al. 2024c) put constraints on the CBD properties using GWs from individual events alone. Degeneracies between disc parameters can be possibly broken by associated EM counterpart observations. Another possibility is to study the population of observed events. Realization of MBHB merger rates at the high end of what is expected for LISA (100’s per year; Amaro-Seoane et al. 2023) would allow us to not only analyze events individually, but also the population and learn underlying properties of source distributions and their environments. This strategy is already employed by ground-based GW detectors to disentangle formation channels for the observed stellar-mass binary BH population (Nishizawa et al. 2016; Breivik et al. 2016; Samsing & D’Orazio 2018; D’Orazio & Samsing 2018; Romero-Shaw et al. 2019, 2020; Zevin et al. 2021; Romero-Shaw et al. 2022).

Here we conduct a quantitative study of the differences between merging MBHBs in the LISA band when driven towards merger via retrograde vs prograde accretion. We show that retrograde configurations yield negative effective spin parameters (χ_{eff} ; Damour 2001) correlated with residual eccentricity near-merger, where both can be readily measured via GW observations. This contrasts with prograde systems and may be unique among formation channels, offering a possibly distinct indicator of the environmental effects that abetted a binary merger.

2 BINARY EVOLUTION MODEL

Consider the motion of two equal-mass spinning BHs of total redshifted mass M_z at redshift z in a bound eccentric orbit with a detector-frame semi-major axis¹ (SMA) a and eccentricity e embedded in a circumbinary disc (CBD). A prograde (retrograde) CBD implies that the disc’s angular momentum (\vec{L}_{CBD}) is in the same (opposite) direction as the binary’s angular momentum (\vec{L}_{Binary}). Moreover, a prograde (retrograde) CBD leads to CBD-aligned mini-discs around each component BH (D’Orazio & Duffell 2021; Tiede & D’Orazio 2024). We also define a dimensionless spin parameter² $s \equiv cJ/Gm^2 \in (-1, 1)$ for a BH of mass m and a spin angular

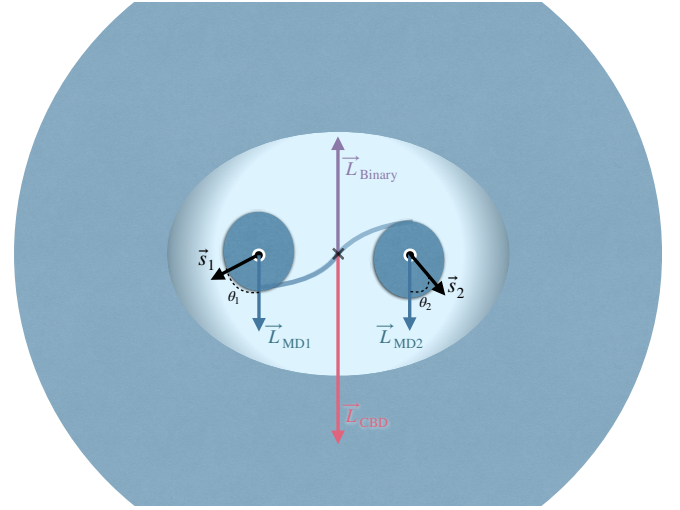


Figure 1. Schematic for a retrograde CBD configuration, where the binary with angular momentum \vec{L}_{Binary} is anti-aligned with that of the accretion disc \vec{L}_{CBD} . The two component BHs have spin vectors $\vec{s}_{1,2}$, which are misaligned by an angle $\theta_{1,2} \in [0, \pi/2)$ with respect to their own CBD-aligned mini-discs of angular momenta $\vec{L}_{\text{MD}1,2}$.

momentum J with positive (negative) values corresponding to a prograde (retrograde) mini-disc orientation with respect to the BH. Fig. 1 shows a schematic for our system for a retrograde CBD configuration.

The quantity s sets the innermost stable circular orbit (ISCO; a_{ISCO}) and radiative efficiency (ϵ) of the accretion onto the BH (Fiacconi et al. 2018):

$$a_{\text{ISCO}} = F(s)Gm/c^2, \quad \epsilon = 1 - \sqrt{1 - 2/3F}, \quad (1)$$

$$F(s) = 3 + Z_2 \mp \sqrt{(3 - Z_1)(3 + Z_1 + 2Z_2)},$$

$$Z_1 = 1 + (1 - s^2)^{\frac{1}{3}} [(1 + s)^{\frac{1}{3}} + (1 - s)^{\frac{1}{3}}], \quad Z_2 = \sqrt{3s^2 + Z_1^2},$$

where upper (lower) sign represents a prograde (retrograde) mini-disc configuration.

The evolution of a spin (s_i) that is fully (anti-) aligned with its co-planar mini-disc (*i.e.*, $\theta_i = 0$) is (Fiacconi et al. 2018)

$$\dot{s}_i = \frac{\dot{M}_{z,i}}{M_{z,i}} \left(\frac{F^2 \mp 2s_i\sqrt{F} + s_i^2}{F\sqrt{F - 3 \pm 2s_i/\sqrt{F}}} \frac{1}{1 - \epsilon_i} - 2s_i \right) = \frac{\dot{M}_{z,i}}{M_{z,i}} \tilde{F}(s_i), \quad (2)$$

where again upper (lower) sign represents a prograde (retrograde) mini-disc orientation and $M_{z,i} = M_z/2$. Here $\dot{M}_{z,i}$ is the accretion rate onto the component BH and determined by the steady-state accretion rate at infinity $\dot{M}_0 \equiv f_{\text{Edd}}M_z/45 \text{ Myr}^{-1}$ (Jiang et al. 2014) via $\dot{M}_{z,i} = (1 - \epsilon_i)\dot{M}_0/2$. Assuming \dot{M}_0 is split evenly between both component BHs, motivated by measured preferential accretion for both prograde and retrograde CBDs (D’Orazio et al. 2024), we can write down the accretion rate onto the binary

$$\dot{M}_z = \left(1 - \frac{\epsilon_1 + \epsilon_2}{2}\right) \dot{M}_0 = \left(1 - \frac{\epsilon_1 + \epsilon_2}{2}\right) \frac{f_{\text{Edd}}}{45 \text{ Myr}} M_z, \quad (3)$$

where f_{Edd} is the Eddington ratio and ϵ_i is the efficiency of the i -th component BH. We assume \dot{M}_0 or equivalently f_{Edd} are constant throughout the binary evolution, *i.e.*, the feeding rate to the disc at infinity is constant.

For an equal-mass MBHB embedded in a co-planar circumbinary disc (CBD), the details of the accretion flow and binary-disc parameters dictate if the gas torques the binary to inspiral or outspiral. For

¹ Detector-frame SMA is $(1 + z)$ times the source-frame SMA, since redshifted orbital frequency $\propto \sqrt{M_z/a^3}$.

² Here G is the gravitational constant and c is the speed of light.

a retrograde disc, the evolution of SMA and eccentricity due to gas are (Tiede & D’Orazio 2024)

$$\dot{a}_{\text{gas}}^{\text{ret}} \approx -10 \frac{\dot{M}_z}{M_z} a, \quad \dot{e}_{\text{gas}}^{\text{ret}} \approx \frac{\dot{M}_z}{M_z} \begin{cases} 20e, & e \leq 0.15, \\ 3, & e > 0.15. \end{cases} \quad (4)$$

While for the prograde binary, we take $e_{\text{gas}}^{\text{pro}}$ from the Zrake et al. (2021) fit and the most negative value of $\dot{a}_{\text{gas}}^{\text{pro}}$ from D’Orazio & Duffell (2021) to consider the fastest merger timescale:

$$\dot{a}_{\text{gas}}^{\text{pro}} = -5 \frac{\dot{M}_z}{M_z} a. \quad (5)$$

We also always initialize prograde binaries from their equilibrium eccentricity $e_{\text{eq}}^{\text{pro}} = 0.45$ (Zrake et al. 2021; D’Orazio & Duffell 2021; Siwek et al. 2023), where binaries only circularize when GW emission becomes dominant over gas effects. This will result in the fastest inspiral times for the prograde case to compare with retrograde results computed later. Slower inspiral times will only exacerbate the differences we later find between the two disc configurations.

GWs remove energy and angular momentum from a compact MBHB. At Newtonian-order, orbit-averaged evolution rates for a and e due to emission of GWs are (Peters & Mathews 1963; Peters 1964)

$$\dot{a}_{\text{GW}} = -\frac{16}{5} \frac{G^3}{c^5} \frac{M_z^3}{a^3} \left(1 + \frac{73}{24} e^2 + \frac{37}{96} e^4 \right) (1 - e^2)^{-\frac{7}{2}}, \quad (6)$$

$$\dot{e}_{\text{GW}} = -e \frac{76}{15} \frac{G^3}{c^5} \frac{M_z^3}{a^4} \left(1 + \frac{121}{304} e^2 \right) (1 - e^2)^{-\frac{5}{2}}.$$

Even though retrograde configurations in § 3 will induce high eccentricities during binary evolution, we have checked that we never reach the relativistic regime to require higher post-Newtonian (PN) terms.

We choose to begin our binary evolution from the self-gravitating radius (R_{sg}) of a thin CBD. Beyond this, the disc can fragment, or calculations including disc self-gravity are required (see, e.g. Franchini et al. 2021). Furthermore, we argue that this is the valid limit for the $M_z \lesssim 10^7$ MBHBs in the LISA band. For a turbulo-viscous parameter $\alpha = 0.1$ (Shakura & Sunyaev 1973), the self-gravitating radius can be expressed as (Perego et al. 2009; Bortolas et al. 2021)

$$R_{\text{sg}}[r_s] = 5.32 \times 10^6 (f_{\text{Edd}}/0.1)^{-\frac{22}{45}} \left(M_z/10^5 M_{\odot} \right)^{-\frac{52}{45}}, \quad (7)$$

where $r_s \equiv 2GM_z/c^2$ is the Schwarzschild radius of the total binary mass. For MBHBs in the LISA band, R_{sg} is much larger than the separation scale where GW inspiral will outpace the CBD and gas effects are no longer important ($a \lesssim 10^2 r_s$; see, e.g. Dittmann et al. 2023). Hence, for the lower-mass LISA MBHBs, we are justified in using Eqs (4) and (5), as a gravitationally stable CBD will surround such MBHBs during a long duration of inspiral where gas effects can dominate over GW-driven evolution. Therefore, we consider earlier evolution of the MBHB via stars or gravitationally unstable gas as setting our initial conditions, which will primarily dictate final values of binary parameters in § 3.

We assume that the binary is always fully (anti-) aligned with its CBD at least by the time the system is initialized at the self-gravitating radius. For mild initial misalignment, it takes around a few Myr for complete (anti-) alignment (Martin & Lubow 2019). Moreover, we assume that the magnitude and misalignment angle of the component BH’s spin vector evolve independently from each other. We also always assume that the BH spins (anti-) align with their minidisks when the binary reaches the LISA band. The spin-alignment timescale is at maximum ~ 60 Myr for an already maximally spinning BH with

almost $\pi/2$ radians misalignment for $f_{\text{Edd}} = 0.1$ and azimuthal Mach number 10 (Lodato & Gerosa 2013). Therefore, for almost all parameters considered, the BH spins will fully align with their mini-discs, and only for a narrow set of parameters will some residual misalignment remain near merger. This can be seen later in Fig. 2, where only for initial eccentricities $e_0 \gtrsim 0.6$, inspiral timescales are less than 60 Myr. Our spin-alignment assumption is further supported by Bourne et al. (2024), where they almost always find spin alignment irrespective of the disc orientation and initial eccentricity.

To study the evolution of binary parameters under the influence of both GWs and CBD, we evolve the following coupled equations from $a = R_{\text{sg}}$ to 1 year before merger³ in the LISA band:

$$\dot{a} = \dot{a}_{\text{GW}} + \dot{a}_{\text{gas}}, \quad \dot{e} = \dot{e}_{\text{GW}} + \dot{e}_{\text{gas}}, \quad (8)$$

$$\frac{\dot{M}_z}{M_z} = \left(1 - \frac{\epsilon_1 + \epsilon_2}{2} \right) \frac{f_{\text{Edd}}}{45 \text{ Myr}}, \quad \dot{s}_1 = \frac{\dot{M}_{z,1}}{M_{z,1}} \tilde{F}(s_1), \quad \& \quad \dot{s}_2 = \frac{\dot{M}_{z,2}}{M_{z,2}} \tilde{F}(s_2),$$

where \dot{a}_{gas} is $\dot{a}_{\text{gas}}^{\text{pro}}$ ($\dot{a}_{\text{gas}}^{\text{ret}}$) for the prograde (retrograde) CBD.

Since we consider long-term evolution under retrograde accretion, it is important to verify that the accretion remains stably anti-aligned throughout the inspiral. If not, the CBD can tilt and eventually align in a prograde configuration (see, e.g. Roedig & Sesana 2014). For a stable evolution, the ratio (f_{st}) between the disc angular momentum (L_{CBD}) and twice the binary angular momentum ($2L_{\text{Binary}}$) needs to be less than unity (King et al. 2005; Nixon et al. 2011b). The binary angular momentum scales with SMA as $L_{\text{Binary}} \propto a^{1/2}$, and the radial dependence of the disc angular momentum L_{CBD} is determined by the surface density profile via the integral $\int_0^{Na} dr \Sigma(r) r^{3/2}$, where $r = Na$ denotes the radius out to which the disc influences the binary. One can see that as long as $\Sigma(r) \propto r^{\gamma}$ has a power-law coefficient $\gamma > -2$, stability will always increase as the binary shrinks at fixed eccentricity. This is the case for our assumed Shakura & Sunyaev (1973) disc in all three regions – inner, middle, and outer – of the disc. We show explicitly that f_{st} for the inner and middle region is always much less than unity in Appendix A, even for high eccentricity, and discuss the outer disc here, as it presents the most stringent stability constraints.

For an equal-mass MBHB (in the source frame) around a thin disc, the stability ratio for the outer disc is⁴

$$f_{\text{st}}^{\text{out}} \sim \frac{0.39}{\sqrt{1-e^2}} \left(\frac{\alpha}{0.1} \right)^{-\frac{4}{5}} \left(\frac{f_{\text{Edd}}}{0.1} \right)^{\frac{7}{10}} \left(\frac{M_z}{10^5 M_{\odot}} \right)^{-\frac{1}{20}} \left(\frac{N}{3} \right)^{\frac{7}{4}} \times \left(\frac{a}{5.32 \times 10^6 r_s} \right)^{\frac{5}{4}}, \quad (9)$$

where we have conservatively chosen a to be the self-gravitating radius for the above reference parameters, $\alpha = 0.1$, $f_{\text{Edd}} = 0.1$, and $M_z = 10^5 M_{\odot}$ (consistent with Schnittman & Krolik (2015)⁵). For the range of parameters we consider in this study, this ratio remains less than unity for $N \lesssim 3$. This is a reasonable value for N given that it is derived at a maximal binary separation, at the self-gravitating radius, and that the majority of torques in the retrograde case come from the flow at $r \lesssim 2a$ (Tiede et al. 2024). Hence, at binary initialization, the stability ratio is less than unity for $e \lesssim 0.9$, consistent

³ SMA, one year before merging, is calculated by integrating \dot{a}_{GW} with final separation a_{ISCO} .

⁴ Even in the source frame, we still keep symbols M_z and a to avoid introducing new ones, and they represent 2–3 times smaller values than their respective redshifted parameters for our considered redshifts of 1 and 2 in §3.

⁵ Once the aspect ratio in their Eq. (26) is converted to include radial coordinate dependence (Haiman et al. 2009, 2022).

with our initialization at $e_0 \leq 0.8$. Then as the binary evolves, the decreased semi-major axis increases stability as eccentricity pumping acts to destabilize. The binary reaches a maximum eccentricity of $e \sim 0.999$ at $a \sim 10^5 r_s$, before GWs circularize the binary, but even at this point the stabilization of the decaying binary dominates and we find $t_{\text{st}}^{\text{out}} \lesssim 1$. Thus, we conclude that the CBD can stably anti-align at the initialization values chosen here, and that it remains stable until at least the point of binary decoupling from the disc, where we end our integration, *i.e.*, we have long-term stable retrograde accretion. This conclusion is in line with previous works, such as Nixon 2012; Schnittman & Krolik 2015 but in contrast with Roedig & Sesana (2014) because they considered more massive (by a factor of $O(10)$) self-gravitating discs.

In the next section, we evolve our systems of interest under the influence of both gas and GWs to find expected binary parameters in the LISA band.

3 RESULTS

3.1 Relevant timescales

We solve the coupled equations in Eq. (8) for the retrograde system for $f_{\text{Edd}} = 0.1$, $z = 1$, an initial total mass $M_{z,0} = 10^5 M_\odot$, initial spins $s_{1,2} = 0$, and for various initial eccentricities e_0 . In Table 1, we show the corresponding inspiral timescale t_{ins} , eccentricity one-year before merger ($e_{1\text{yr}}$), the final-to-initial total-mass ratio, and final spins. Here, $M_z/M_{z,0}$ can be well approximated by $\exp(f_{\text{Edd}} t_{\text{ins}}/50 \text{ Myr})$. The retrograde accretion leads to higher residual eccentricities, which should be measurable in the LISA band (Garg et al. 2024b,c). We can also infer from $s_{1,2} > 0$ that retrograde accretion leads to component BH spins aligned with their mini-discs and anti-aligned with the binary. Increasing the total mass to $M_{z,0} = 10^6 M_\odot$ does not meaningfully alter t_{ins} for retrograde binaries,⁶ but $e_{1\text{yr}}$ decreases by a factor of 5 from the $M = 10^5 M_\odot$ case for a given e_0 . While for a prograde binary, $e_{1\text{yr}} \sim 10^{-3}$, irrespective of the initial total mass. Increasing the accretion rate to $f_{\text{Edd}} = 1$ results in a nearly ten times faster inspiral time as well as slightly higher eccentricities for retrograde CBDs and $e_{1\text{yr}} \sim 10^{-2.5}$ for prograde scenarios. We note that previous works have also found trends in eccentricity for prograde vs retrograde consistent with our models (Roedig et al. 2011; Schnittman & Krolik 2015; Zrake et al. 2021). While the final spins are almost independent of f_{Edd} , we further discuss spin evolution in § 3.2.

In Fig. 2, as a function of e_0 , we compare spin-up timescales from different initial spin magnitudes, binary lifetimes for different configurations, and a typical CBD lifetime based on observations of AGN. We see that the prograde systems live longer than their spin-up timescales for any s_0 , while retrograde systems have lifespans shorter than the spin-up timescale. This implies that prograde systems will always maximally spin up their component BHs to align with the orbital angular momentum (Dotti et al. 2010) while in retrograde scenarios this happens only for initially highly spinning component BHs aligned with their minidisks (and so anti-aligned with the binary, *i.e.*, $s_0 \sim 1$). We further explore retrograde spin-up in the next subsection.

The observationally motivated CBD lifetime for $f_{\text{Edd}} \gtrsim 0.1$ is around 100 Myr (Hopkins & Hernquist 2009), for masses relevant to LISA. This implies that for $f_{\text{Edd}} = 0.1$, MBHBs initialized from the self-gravitating radius with either prograde CBDs or retrograde

e_0	t_{ins} [Myr]	$e_{1\text{yr}}$	$M_z/M_{z,0}$	$s_{1,2}$
0	370	0	2.03	0.99
0.1	149	0.03	1.35	0.73
0.2	130	0.05	1.31	0.67
0.3	113	0.06	1.26	0.62
0.4	97	0.09	1.22	0.55
0.5	81	0.12	1.18	0.48
0.6	64	0.16	1.14	0.41
0.7	48	0.21	1.11	0.32
0.8	32	0.27	1.07	0.22

Table 1. The initial eccentricity (e_0), the inspiral timescale (t_{ins}), the eccentricity one year before merger ($e_{1\text{yr}}$), the final-to-initial total mass ratio, and final spins assuming $f_{\text{Edd}} = 0.1$, initial total mass $M_{z,0} = 10^5 M_\odot$, and zero initial spins, for retrograde evolution.

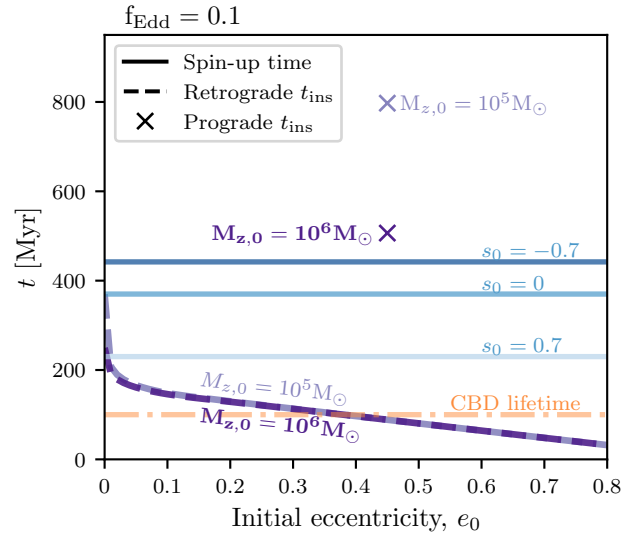


Figure 2. Timescales of interest for $f_{\text{Edd}} = 0.1$ as a function of initial eccentricity e_0 . We show inspiral timescales (dashed lines) for two initial total masses $M_{z,0} = 10^5 M_\odot$ (light purple) and $M_{z,0} = 10^6 M_\odot$ (dark purple) in a retrograde CBD starting from the self-gravitating radius of the disc. For comparison, we show prograde results (\times 's) for the same masses initialized at $e_0 = 0.45$. We also show spin-up timescales (solid lines) for a component BH to increase its spin to $s_i = 0.99$ from three initial spins. We draw an expected, 100 Myr, CBD lifetime as the dot-dashed orange line.

CBDs with low initial binary eccentricity ($e_0 \lesssim 0.3$) will not reach the LISA band in the absence of other hardening mechanisms. To consider this, § 3.3 shows population results for three scenarios: no restriction on inspiral timescale, $t_{\text{ins}} \lesssim 100$ Myr restriction by starting longer inspiral systems closer than R_{sg} , and only considering R_{sg} initialized MBHBs that merge within the CBD lifetime, *i.e.*, $t_{\text{ins}}^{\text{sg}} < 100$ Myr.

3.2 Spin evolution

Despite retrograde binary lifetimes being shorter than the typical spin-up time, a significant imprint on the effective spin in the LISA band can still arise for retrograde systems.

The effective spin of the binary χ_{eff} assuming complete (anti-)

⁶ Except for $e_0 = 0$ case, where $t_{\text{ins}} \sim 250$ Myr.

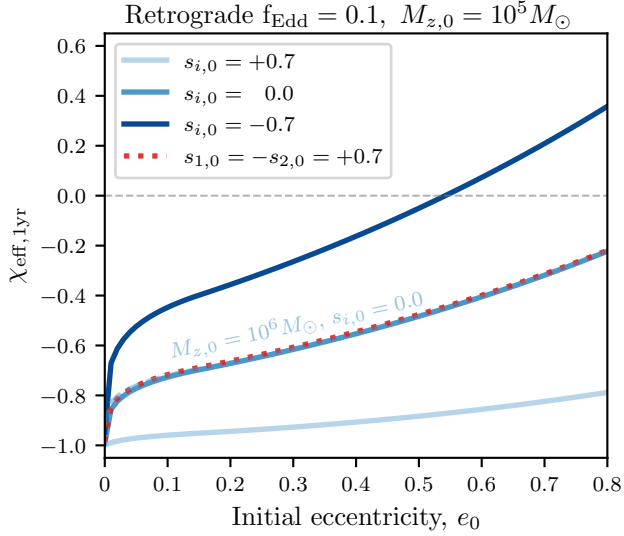


Figure 3. Effective spin $\chi_{\text{eff},1\text{yr}}$, one year before merger for a $M_{z,0} = 10^5 M_{\odot}$ (solid line) MBHB with $f_{\text{Edd}} = 0.1$ retrograde CBD, as a function of the initial eccentricity e_0 for different initial spin configurations. We also include $M_{z,0} = 10^6 M_{\odot}$ (dashed medium blue) with zero initial spins for comparison.

alignment is (Damour 2001)

$$\chi_{\text{eff}} = \frac{s_1 + s_2}{2} \times \begin{cases} +1, & \text{for prograde CBD,} \\ -1, & \text{for retrograde CBD.} \end{cases} \quad (10)$$

Fig. 3 plots the expected effective spin one-year before merger ($\chi_{\text{eff},1\text{yr}}$) for retrograde evolution for a few systems of interests. Low initial eccentricities lead to longer inspiral timescales (see Fig. 2), allowing more time for the mini-discs to spin-up the BHs, resulting in more negative $\chi_{\text{eff},1\text{yr}}$ for retrograde binaries.

3.3 Population

We are interested in estimating the expected distribution for the effective spin ($\chi_{\text{eff},1\text{yr}}$) and the eccentricity ($e_{1\text{yr}}$), one-year before merger, when LISA can probe it. To do so we realize a population by drawing the parameters described in Sec. 2 as follows:

- For initial total masses, we relate $M_{z,0}$ to the MBHB’s luminosity $L = f_{\text{Edd}} L_{\text{Edd}}$, where the Eddington luminosity $L_{\text{Edd}} \equiv 6.3 \times 10^4 M_{z,0} \text{ ergs g}^{-1} \text{ s}^{-1}$ and then draw L from the observed quasar luminosity function (QLF) at redshifts $z = 1$ and $z = 2$ (Hopkins et al. 2007). We choose these low redshifts because that’s where we expect the highest-SNR MBHB mergers and the most likely candidates for multi-messenger detections (see, e.g. Mangiagli et al. 2022). The latter would be particularly helpful in constraining disc properties (Garg et al. 2024c). We are also more likely to detect low eccentricities (Garg et al. 2024b) and well-measured effective spins for high-SNR MBHBs as compared to sources at further distances. The former requires $\text{SNR} \gtrsim 10$ during inspiral, which is typically $\sim 5\%$ of the total event SNR, which is only possible for low-redshift MBHBs. Moreover, to have events in the LISA band, we only consider initial total masses $M_{z,0} \sim [10^{4.5}, 10^7] M_{\odot}$ for retrograde MBHBs and $M_{z,0} \sim [10^4, 10^7] M_{\odot}$ for prograde MBHBs. Different initial mass ranges are needed to get the same distribution of total masses $\sim [10^{4.5}, 10^{7.5}] M_{\odot}$ in the LISA band since the prograde inspiral timescale is much longer than in the retrograde case leading to larger increases in mass.

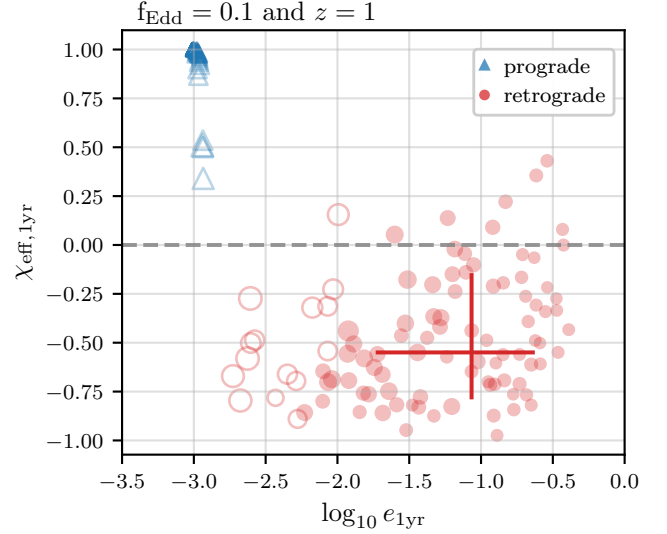


Figure 4. $\chi_{\text{eff},1\text{yr}}$ vs $e_{1\text{yr}}$ for 100 LISA-observable MBHBs at $z = 1$ for prograde (blue triangles) and retrograde (red circles) CBDs with $f_{\text{Edd}} = 0.1$ Eddington ratio. The marker size represents how large M_z is in the range $\sim [10^{4.5}, 10^{7.5}] M_{\odot}$. Filled symbols corresponds to measurable eccentricity ($e_{1\text{yr}}^{\text{det}}$) as per Garg et al. (2024b,c). For retrograde systems, we draw solid red bars indicating 68 per cent credible intervals of spin-eccentricity distribution for measurable eccentricity events with intersection indicating median values

- We draw initial spin magnitudes and eccentricities from uniform distributions: $s_0 \sim \text{Uniform}(-1, 1)$ and $e_0 \sim \text{Uniform}(0, 0.8)$.

We initialized 100 MBHBs from their CBD’s self-gravitating radius, such that all events have SNR of at least 8 at $z = 1$ in the LISA band to be observable (Garg et al. 2022) and to mimic expected MBHB detections by LISA (Amaro-Seoane et al. 2023). For both retrograde and prograde MBHBs, we show $\chi_{\text{eff},1\text{yr}}$ vs $e_{1\text{yr}}$ in Fig. 4 at redshift $z = 1$ and $f_{\text{Edd}} = 0.1$. We find that prograde CBDs lead to almost positive unity effective spin and non-measurable $e_{1\text{yr}}$,⁷ and in the retrograde case, we mostly have negative $\chi_{\text{eff},1\text{yr}}$ and measurable eccentricities.⁸

Assuming all binaries are brought to merger by an accretion phase, Fig. 4 shows that one could distinguish between prograde and retrograde from their $\chi_{\text{eff},1\text{yr}}$ vs $e_{1\text{yr}}$ correlations in the LISA band, as they occupy different parts of the parameter space. Note that, even for the fastest inspiral case in prograde, we predict almost unity effective spin such that this should also be the case for more complex evolutions $a_{\text{gas}}^{\text{pro}}$ (see, e.g. D’Orazio & Duffell 2021). Similarly, $e_{1\text{yr}}$ for prograde scenarios should be the same for equal-mass MBHBs (Zrake et al. 2021) as it is only a function of the equilibrium value $e_{\text{eq}}^{\text{pro}} = 0.45$ (see also Siwek et al. 2023; Valli et al. 2024). Thus we expect that our prograde results are robust despite the simplifications.

In Fig. 5, we repeat this experiment for 10^4 LISA-observable events for varying scenarios to better ascertain the underlying distributions and minimize variance from drawing fewer events. In comparison to our fiducial retrograde case with Eddington ratio $f_{\text{Edd}} = 0.1$ and redshift $z = 1$, we consider $f_{\text{Edd}} = 1$, $z = 2$, and CBD-lifetime restricted

⁷ However, for prograde accretion with $f_{\text{Edd}} = 1$, we expect measurable eccentricities $e_{1\text{yr}} \sim 10^{-2.5}$ for $M_z \lesssim 10^5 M_{\odot}$.

⁸ An equal-mass merging MBHB with $M_z = 10^5 M_{\odot}$ has the minimum measurable eccentricity $10^{-2.75}$ at $z = 1$ for a one-year observation window (Garg et al. 2024c).

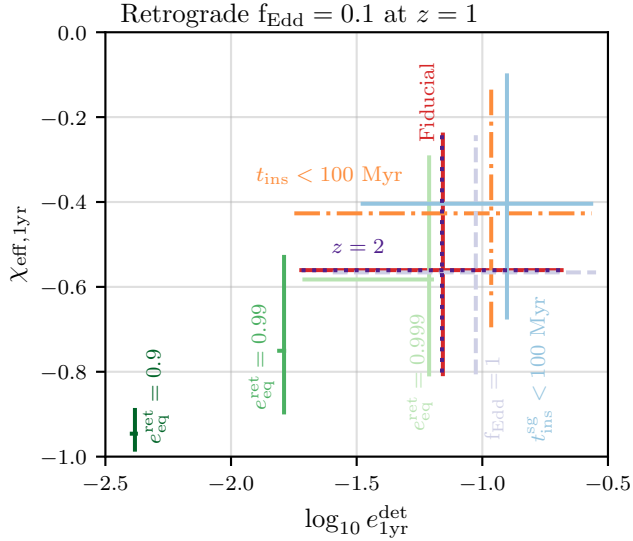


Figure 5. Spin-eccentricity correlations for MBHBs with detectable eccentricity ($e_{1\text{yr}}^{\text{det}}$) for different scenarios in comparison to our fiducial retrograde CBD (solid red) with $f_{\text{Edd}} = 0.1$ at $z = 1$. We show $f_{\text{Edd}} = 1$ (dashed light purple), $z = 2$ (dotted dark purple), $t_{\text{ins}} < 100$ Myr (dot-dashed orange), $t_{\text{ins}}^{\text{sg}} < 100$ Myr (solid medium blue), and assuming the maximum eccentricity in retrograde ($e_{\text{eq}}^{\text{ret}}$) to be either 0.9 (solid dark green), 0.99 (solid medium green), and 0.999 (solid light green). Bars are similar to Fig. 4 and we summarize these bounds in Table 2.

Scenario	$\log_{10} e_{1\text{yr}}^{\text{det}}$	$\chi_{\text{eff},1\text{yr}}$
Fiducial	$-1.16^{+0.48}_{-0.57}$	$-0.56^{+0.32}_{-0.25}$
$f_{\text{Edd}} = 1$	$-1.03^{+0.48}_{-0.57}$	$-0.57^{+0.32}_{-0.24}$
$z = 2$	$-1.16^{+0.48}_{-0.56}$	$-0.56^{+0.33}_{-0.24}$
$t_{\text{ins}} < 100$ Myr	$-0.96^{+0.40}_{-0.76}$	$-0.43^{+0.30}_{-0.27}$
$t_{\text{ins}}^{\text{sg}} < 100$ Myr	$-0.90^{+0.34}_{-0.58}$	$-0.40^{+0.31}_{-0.27}$
$e_{\text{eq}}^{\text{ret}} = 0.9$	$-2.38^{+0.01}_{-0.02}$	$-0.95^{+0.06}_{-0.04}$
$e_{\text{eq}}^{\text{ret}} = 0.99$	$-1.79^{+0.01}_{-0.03}$	$-0.75^{+0.23}_{-0.15}$
$e_{\text{eq}}^{\text{ret}} = 0.999$	$-1.21^{+0.02}_{-0.50}$	$-0.58^{+0.29}_{-0.23}$

Table 2. Measurable eccentricity ($e_{1\text{yr}}^{\text{det}}$) and effective spin distributions for different scenarios in Fig. 5.

inspirals: either $t_{\text{ins}} < 100$ Myr or only considering events which merge with $t_{\text{ins}}^{\text{sg}} < 100$ Myr, when initialized from the self-gravity radius. We also consider different maximum equilibrium eccentricities (dubbed $e_{\text{eq}}^{\text{ret}}$) for the retrograde CBD. That is to say, one might imagine that retrograde discs can only pump eccentricity to some maximum value $e_{\text{eq}}^{\text{ret}}$ at which shock-dissipation at pericenter (or some other mechanism) could shut off eccentricity growth. In such a scenario, the MBHB will stall at $e_{\text{eq}}^{\text{ret}}$, keep shrinking due to $\dot{a}_{\text{gas}}^{\text{ret}}$, and will circularize when GWs become dominant. Lowering $e_{\text{eq}}^{\text{ret}}$ results in longer inspiral timescales and more negative $\chi_{\text{eff},1\text{yr}}$, but smaller $e_{1\text{yr}}^{\text{det}}$. We note, however, that each of these scenarios in Fig. 5 retains an in-band eccentricity above the $e_{1\text{yr}} > 10^{-2.75}$ detection threshold for an equal-mass $10^5 M_{\odot}$ binary.

Both redshifts produce similar spin-eccentricity correlations, implying that our results are independent of redshift. This is because once we consider detector-frame quantities, a fixed range for total

masses $M_z \sim [10^{4.5}, 10^{7.5}] M_{\odot}$, and the same number of observable events, then only QLF, SNR, and the minimum measurable eccentricity changes with redshift. QLF’s shape depends weakly on z , SNRs are still higher than our threshold of 8 at $z = 2$, and the minimum measurable eccentricity only increases slightly at $z = 2$, effectively, not changing results at different redshifts. While spin distributions are almost the same for both Eddington ratios $f_{\text{Edd}} = 0.1$ and $f_{\text{Edd}} = 1$, $e_{1\text{yr}}^{\text{det}}$ is slightly higher for the latter and this could help to distinguish between Eddington ratios.⁹ Limiting the inspiral timescale to typical AGN lifetimes of 100 Myr leads to higher effective spin and higher measurable eccentricities. The former is because smaller initial eccentricities are time limited and not able to spin BHs to high negative effective spin as per Figs 2 and 3 and the latter because higher initial eccentricities are selected because they merge more quickly.

4 DISCUSSION AND CONCLUSION

We find that MBHBs with a retrograde CBD typically have negative effective spin and measurable eccentricity in the LISA band. This is in contrast to prograde scenarios, which result in positive effective spin and smaller or non-measurable $e_{1\text{yr}}$. Moreover, the spin-eccentricity distribution of binaries evolving through a retrograde accretion channel occupy a unique part of parameter space that appears to be robust to environmental or evolutionary parameters such as f_{Edd} , redshift, or $e_{\text{eq}}^{\text{ret}}$. However, different parameters could change the exact quantitative spin-eccentricity correlations, which may update with advances in simulating CBD-driven orbital evolution.

A binary carried to merger via retrograde accretion (with $f_{\text{Edd}} \geq 0.1$) should have a unique observable signature in the gravitational waveform with a negative effective spin and a detectable eccentricity. This would likely come in combination with a measurable negative GW-phase perturbation at the -4PN order due to secular gas effects in the orbital evolution (Garg et al. 2024c). This would provide a strong clue for distinguishing between binary hardening mechanisms in the LISA band (see, e.g. Zwick et al. 2023).

Chaotic accretion (or similarly many different accretion events leading up to merger, with differing disc alignments) typically leads to low-spin MBHBs near merger (King et al. 2008; Chen & Lin 2023), which could also be the case for some retrograde MBHBs as shown in Fig. 4 but not for the prograde accretion. However, a measurable eccentricity should help in distinguishing retrograde from frequent chaotic accretion, as the latter may not have enough accretion to either pump eccentricities similar to retrograde or sustain equilibrium eccentricity as in prograde. But this needs to be shown via simulations that if a long-term evolution under chaotic accretion can lead to residual measurable $e_{1\text{yr}}$. Also, measurable -4PN -order GW-phase shifts should help to differentiate retrograde accretion from hardening via a third MBH (Bonetti et al. 2019), which can also excite high residual eccentricities in the LISA band. Moreover, a CBD leads to an aligned spinning binary while hardening via a third MBH typically forms precessing MBHBs near-merger. Additionally, if we detect an EM counterpart for an MBHB that confirms the presence of an accretion disc (see, e.g. Haiman et al. 2009), then the measured effective spin can provide evidence for the disc orientation.

We have relied on a number of assumptions that might be improved upon in the future. While the hydrodynamical simulation

⁹ For prograde case, $f_{\text{Edd}} = 1$ still has unity $\chi_{\text{eff},1\text{yr}}$ but $e_{1\text{yr}} \sim 10^{-2.5}$ instead of $e_{1\text{yr}} \sim 10^{-3}$ for 0.1 Eddington ratio.

results in Tiede & D’Orazio (2024) are only computed for eccentricity up to 0.8, we extrapolate them to higher eccentricities. Furthermore, existing hydrodynamical results that span a sufficient range of orbital eccentricities derive from 2D, isothermal hydrodynamical treatments of the CBD. While the key ingredients of retrograde eccentricity pumping (for, e.g., 3D, self-gravitating discs, including magnetic fields, or unequal masses Nixon et al. 2011a; Roedig & Sesana 2014; Bankert et al. 2015; Amaro-Seoane et al. 2016) and retrograde mini-discs (Tiede & D’Orazio 2024) appear to be robust, inclusion of more complete physics – e.g. radiative transfer, general relativistic disc-response – in future simulations will be necessary to improve the accuracy of the predictions presented here. Additionally, we add evolution rates from gas and GWs linearly as its not possible to infer cross terms from current simulations for MBHBs. However, studies by Derdzinski et al. (2019, 2021) suggest that for extreme mass ratio inspirals cross terms should be weak, which may also extend to MBHBs. Even though we checked that our systems are never at small enough binary separation to require relativistic corrections, Peters (1964) may still breakdown for extremely high eccentricities due to apsidal precession inducing small but possibly non-negligible error. However, this is not clear how it will affect our results and we leave this for future work. We additionally only consider equal-mass MBHBs, due to the limitation of retrograde results and under the assumption that before reaching the self-gravitating radius the binary has become close to equal-mass through preferential accretion. Lastly, typical hierarchical clustering models suggest that most MBHB mergers may happen at redshifts larger than $z = 2$ (see, e.g. Barausse 2012; Bonetti et al. 2019), implying that the number of events may not be enough to do population inference.

In summary, we have demonstrated a possibly unique signature of the retrograde CBD accretion channel comprising MBHB mergers with negative effective spin and measurable eccentricities. This can help to distinguish between the various scenarios—accretion, stellar hardening, and third-body interactions—that enable massive binaries to merge within the lifetime of the universe.

DATA AVAILABILITY STATEMENT

The data underlying this article will be shared on reasonable request to the authors.

ACKNOWLEDGEMENTS

MG acknowledge support from the Swiss National Science Foundation (SNSF) under the grant 200020_192092. D.J.D. and C.T. received support from the Danish Independent Research Fund through Sapere Aude Starting grant No. 121587. C.T. also received support from European Union’s Horizon 2023 research and innovation program under Marie Skłodowska-Curie grant agreement No. 101148364. We thank the anonymous referee for helpful comments that improved this work. The authors also acknowledge use of the NumPy (Harris et al. 2020) and Matplotlib (Hunter 2007).

REFERENCES

- Agazie G., et al., 2023, *ApJ*, **951**, L8
- Amaro-Seoane P., Maureira-Fredes C., Dotti M., Colpi M., 2016, arXiv.org, p. arXiv:1604.01392
- Amaro-Seoane P., et al., 2017, arXiv e-prints, p. arXiv:1702.00786
- Amaro-Seoane P., et al., 2023, *Living Reviews in Relativity*, **26**, 2
- Bankert J., Krolik J. H., Shi J., 2015, *The Astrophysical Journal*, **801**, 114
- Barausse E., 2012, *MNRAS*, **423**, 2533
- Bardeen J. M., 1970, *Nature*, **226**, 64
- Bardeen J. M., Petterson J. A., 1975, *ApJ*, **195**, L65
- Begelman M. C., Blandford R. D., Rees M. J., 1980, *Nature*, **287**, 307
- Blaes O., Lee M. H., Socrates A., 2002, *ApJ*, **578**, 775
- Bonetti M., Sesana A., Haardt F., Barausse E., Colpi M., 2019, *MNRAS*, **486**, 4044
- Bortolas E., Franchini A., Bonetti M., Sesana A., 2021, *ApJ*, **918**, L15
- Bourne M. A., Fiacconi D., Sijacki D., Piotrowska J. M., Koudmani S., 2024, *MNRAS*,
- Breivik K., Rodriguez C. L., Larson S. L., Kalogera V., Rasio F. A., 2016, *ApJ*, **830**, L18
- Chen Y.-X., Lin D. N. C., 2023, *MNRAS*, **522**, 319
- Cocchiararo F., Franchini A., Lupi A., Sesana A., 2024, arXiv e-prints, p. arXiv:2402.05175
- Colpi M., et al., 2024, arXiv e-prints, p. arXiv:2402.07571
- D’Orazio D. J., Charisi M., 2023, arXiv e-prints, p. arXiv:2310.16896
- D’Orazio D. J., Duffell P. C., 2021, *ApJ*, **914**, L21
- D’Orazio D. J., Samsing J., 2018, *MNRAS*, **481**, 4775
- D’Orazio D. J., Haiman Z., Duffell P., MacFadyen A. I., Farris B. D., 2016, *Mon. Not. Roy. Astron. Soc.*, **459**, 2379
- D’Orazio D. J., Duffell P. C., Tiede C., 2024, arXiv e-prints, p. arXiv:2403.05629
- Damour T., 2001, *Phys. Rev. D*, **64**, 124013
- Derdzinski A. M., D’Orazio D., Duffell P., Haiman Z., MacFadyen A., 2019, *MNRAS*, **486**, 2754
- Derdzinski A., D’Orazio D., Duffell P., Haiman Z., MacFadyen A., 2021, *MNRAS*, **501**, 3540
- Dittmann A. J., Ryan G., Miller M. C., 2023, *ApJ*, **949**, L30
- Dotti M., Volonteri M., Perego A., Colpi M., Ruzsowski M., Haardt F., 2010, *MNRAS*, **402**, 682
- EPTA Collaboration et al., 2023, *A&A*, **678**, A50
- Farris B. D., Duffell P., MacFadyen A. I., Haiman Z., 2014, *ApJ*, **783**, 134
- Fiacconi D., Sijacki D., Pringle J. E., 2018, *MNRAS*, **477**, 3807
- Franchini A., Sesana A., Dotti M., 2021, *MNRAS*, **507**, 1458
- Franchini A., Bonetti M., Lupi A., Sesana A., 2024, *A&A*, **686**, A288
- Fumagalli G., Gerosa D., 2023, *Phys. Rev. D*, **108**, 124055
- Garg M., Derdzinski A., Zwick L., Capelo P. R., Mayer L., 2022, *MNRAS*, **517**, 1339
- Garg M., Sberna L., Speri L., Duque F., Gair J., 2024a, arXiv e-prints, p. arXiv:2410.02910
- Garg M., Tiwari S., Derdzinski A., Baker J. G., Marsat S., Mayer L., 2024b, *MNRAS*, **528**, 4176
- Garg M., Derdzinski A., Tiwari S., Gair J., Mayer L., 2024c, *MNRAS*, **532**, 4060
- Gong X., Xu S., Gui S., Huang S., Lau Y.-K., 2021, in , *Handbook of Gravitational Wave Astronomy*. Springer Singapore, p. 24, doi:10.1007/978-981-15-4702-7_24-1
- Gualandris A., Khan F. M., Bortolas E., Bonetti M., Sesana A., Berczik P., Holley-Bockelmann K., 2022, *MNRAS*, **511**, 4753
- Haiman Z., 2017, *Phys. Rev. D*, **96**, 023004
- Haiman Z., Kocsis B., Menou K., 2009, *ApJ*, **700**, 1952
- Haiman Z., Kocsis B., Menou K., 2022, *ApJ*, **937**, 129
- Harris C. R., et al., 2020, *Nature*, **585**, 357
- Hopkins P. F., Hernquist L., 2009, *ApJ*, **698**, 1550
- Hopkins P. F., Richards G. T., Hernquist L., 2007, *ApJ*, **654**, 731
- Hunter J. D., 2007, *Computing in Science & Engineering*, **9**, 90
- Jiang Y.-F., Stone J. M., Davis S. W., 2014, *ApJ*, **796**, 106
- Khan F. M., Just A., Merritt D., 2011, *ApJ*, **732**, 89
- King A. R., Lubow S. H., Ogilvie G. I., Pringle J. E., 2005, *MNRAS*, **363**, 49
- King A. R., Pringle J. E., Hofmann J. A., 2008, *MNRAS*, **385**, 1621
- Li E.-K., et al., 2024, arXiv e-prints, p. arXiv:2409.19665
- Liu B., Lai D., 2017, *ApJ*, **846**, L11
- Lodato G., Gerosa D., 2013, *MNRAS*, **429**, L30
- Mangiagli A., Caprini C., Volonteri M., Marsat S., Vergani S., Tamanini N., Inchauspé H., 2022, *Phys. Rev. D*, **106**, 103017
- Martin R. G., Lubow S. H., 2019, *MNRAS*, **490**, 1332
- Miller M. C., Krolik J. H., 2013, *ApJ*, **774**, 43

Milosavljevic M., Merritt D., 2003, *AIP Conf. Proc.*, 686, 201
 Muñoz D. J., Miranda R., Lai D., 2019, *ApJ*, 871, 84
 Nishizawa A., Berti E., Klein A., Sesana A., 2016, *Phys. Rev. D*, 94, 064020
 Nixon C. J., 2012, *MNRAS*, 423, 2597
 Nixon C. J., Cossins P. J., King A. R., Pringle J. E., 2011a, *MNRAS*, 412, 1591
 Nixon C. J., King A. R., Pringle J. E., 2011b, *MNRAS*, 417, L66
 Perego A., Dotti M., Colpi M., Volonteri M., 2009, *MNRAS*, 399, 2249
 Peters P. C., 1964, PhD thesis, California Institute of Technology
 Peters P. C., Mathews J., 1963, *Physical Review*, 131, 435
 Preto M., Berentzen I., Berczik P., Spurzem R., 2011, *ApJ*, 732, L26
 Quinlan G. D., 1996, *New Astron.*, 1, 35
 Reardon D. J., et al., 2023, *ApJ*, 951, L6
 Roedig C., Sesana A., 2014, *MNRAS*, 439, 3476
 Roedig C., Dotti M., Sesana A., Cuadra J., Colpi M., 2011, *MNRAS*, 415, 3033
 Romero-Shaw I. M., Lasky P. D., Thrane E., 2019, *MNRAS*, 490, 5210
 Romero-Shaw I., Lasky P. D., Thrane E., Calderón Bustillo J., 2020, *ApJ*, 903, L5
 Romero-Shaw I., Lasky P. D., Thrane E., 2022, *ApJ*, 940, 171
 Samsing J., D’Orazio D. J., 2018, *MNRAS*, 481, 5445
 Schnittman J. D., Krolik J. H., 2015, *ApJ*, 806, 88
 Shakura N. I., Sunyaev R. A., 1973, *A&A*, 500, 33
 Siwek M., Weinberger R., Hernquist L., 2023, *MNRAS*, 522, 2707
 Thorne K. S., 1974, *ApJ*, 191, 507
 Tiede C., D’Orazio D. J., 2024, *MNRAS*, 527, 6021
 Tiede C., D’Orazio D. J., Zwick L., Duffell P. C., 2024, *ApJ*, 964, 46
 Valli R., et al., 2024, *A&A*, 688, A128
 Vasiliev E., Antonini F., Merritt D., 2015, *ApJ*, 810, 49
 Xu H., et al., 2023, *Research in Astronomy and Astrophysics*, 23, 075024
 Zevin M., Romero-Shaw I. M., Kremer K., Thrane E., Lasky P. D., 2021, *ApJ*, 921, L43
 Zrake J., Tiede C., MacFadyen A., Haiman Z., 2021, *ApJ*, 909, L13
 Zwick L., Capelo P. R., Mayer L., 2023, *MNRAS*, 521, 4645

4100 $(f_{\text{Edd}}/0.1)^{2/3}$, and for $\epsilon \sim 0.1$:¹⁰

$$f_{\text{st}}^{(\text{I})}(a) \sim \frac{1.85 \times 10^{-6}}{\sqrt{1-e^2}} \left(\frac{\alpha}{0.1}\right)^{-1} \left(\frac{f_{\text{Edd}}}{0.1}\right)^{-1} \left(\frac{M_z}{10^5 M_\odot}\right)^{-\frac{5}{2}} \left(\frac{a}{500 r_s}\right)^{\frac{7}{2}}, \quad (\text{A3})$$

$$f_{\text{st}}^{(\text{II})}(a) \sim \frac{1.46 \times 10^{-5}}{\sqrt{1-e^2}} \left(\frac{\alpha}{0.1}\right)^{-\frac{4}{5}} \left(\frac{f_{\text{Edd}}}{0.1}\right)^{\frac{3}{5}} \left(\frac{M_z}{10^5 M_\odot}\right)^{-\frac{1}{5}} \left(\frac{a}{5000 r_s}\right)^{\frac{7}{5}},$$

$$f_{\text{st}}^{(\text{III})}(a) \sim \frac{0.39}{\sqrt{1-e^2}} \left(\frac{\alpha}{0.1}\right)^{-\frac{4}{5}} \left(\frac{f_{\text{Edd}}}{0.1}\right)^{\frac{7}{10}} \left(\frac{M_z}{10^5 M_\odot}\right)^{-\frac{1}{20}} \left(\frac{N}{3}\right)^{\frac{7}{4}} \left(\frac{a}{5.32 \times 10^6 r_s}\right)^{\frac{5}{4}},$$

where we have normalized a by a multiplier of r_s larger than respective regions of validity up to the self-gravitating radius for the outer disc. Given that $f_{\text{st}}^{(\text{I})} \ll f_{\text{st}}^{(\text{II})} \ll f_{\text{st}}^{(\text{III})}$, we have

$$f_{\text{st}}^{\text{in}} \sim f_{\text{st}}^{(\text{I})}(a), \quad (\text{A4})$$

$$f_{\text{st}}^{\text{mid}} \sim f_{\text{st}}^{(\text{II})}(a),$$

$$f_{\text{st}}^{\text{out}} \sim f_{\text{st}}^{(\text{III})}(a).$$

All three regions are stable for our parameters of interest.

This paper has been typeset from a $\text{\TeX}/\text{\LaTeX}$ file prepared by the author.

APPENDIX A: STABILITY OF RETROGRADE ACCRETION

The accretion stability ratio, *i.e.*, $L_{\text{CBD}} = 2\pi \int_0^{Na} r dr \Sigma(r) \sqrt{GM_z r}$ divided by $2L_{\text{Binary}} = 2M_z \sqrt{GM_z a(1-e^2)}/4$, is

$$f_{\text{st}} = \frac{L_{\text{CBD}}}{2L_{\text{Binary}}} = 4\pi \frac{\int_0^{Na} dr \Sigma(r) r^{\frac{3}{2}}}{M_z \sqrt{a(1-e^2)}}. \quad (\text{A1})$$

Depending on the radial coordinate, we can divide the Shakura & Sunyaev (1973) disc into three regions - inner, middle, and outer - with different respective surface density profiles (Haiman et al. 2009, 2022). Substituting into Eq. (A1) gives

$$f_{\text{st}}^{\text{in}}(a) = f_{\text{st}}^{(\text{I})}(a), \quad a \lesssim N_1 r_s, \quad (\text{A2})$$

$$f_{\text{st}}^{\text{mid}}(a) = f_{\text{st}}^{(\text{I})}(N_1 r_s) + f_{\text{st}}^{(\text{II})}(a), \quad N_1 r_s \lesssim a \lesssim N_2 r_s,$$

$$f_{\text{st}}^{\text{out}}(a) = f_{\text{st}}^{(\text{I})}(N_1 r_s) + f_{\text{st}}^{(\text{II})}(N_2 r_s) + f_{\text{st}}^{(\text{III})}(a), \quad N_2 r_s \lesssim a \lesssim Na,$$

where $N_1 \ll 299 (f_{\text{Edd}}/0.1)^{16/21} (M_z/10^5 M_\odot)^{2/21}$, $N_2 \sim$

¹⁰ We ignore the lower integration limit as it is much smaller than the upper limit for simplicity.